



Repositorio Institucional de la Universidad Autónoma de Madrid

<https://repositorio.uam.es>

Esta es la **versión de autor** del artículo publicado en:
This is an **author produced version** of a paper published in:

Solar Energy Materials and Solar Cells 186 (2018): 115-123

DOI: <https://doi.org/10.1016/j.solmat.2018.06.015>

Copyright: © 2018 Elsevier B.V. All rights reserved.

El acceso a la versión del editor puede requerir la suscripción del recurso

Access to the published version may require subscription

Sulfurization of co-evaporated $\text{Cu}_2\text{ZnSnSe}_4$ thin film solar cells: The role of Na.
L. de la Cueva^{a*}, Y. Sánchez^b, L. Calvo-Barrio^c, F. Oliva^b, V. Izquierdo-Roca^b, S.
Khelifi^{d,e}, T. Bertram^f, J.M. Merino^a, M. León^a, R. Caballero^{a*}

^aUniversidad Autónoma de Madrid, Departamento de Física Aplicada, C/ Francisco Tomás y Valiente 7, 28049 Madrid, Spain

^bIREC, Catalonia Institute for Energy Research, C/ Jardins de les Dones de Negre 1, Sant Adrià del Besòs, 08930 Barcelona, Spain

^cCentres Científics i Tecnològics (CCiTUB) i Departament d'Enginyeria Electrònica i Biomèdica de la Universitat de Barcelona, C/ Lluís Solé i Sabaris, 08028 Barcelona, Spain

^dDepartment of Electronics and Information Systems (ELIS), Gent University, iGent tower, Technology Park 15, Zwijnaarde 9052 Gent, Belgium

^eDepartment of Solid State Sciences, Krijgslaan 281-S1, 9000 Gent, Belgium

^fPVcomB, Helmholtz-Zentrum Berlin, Schwarzschildstraße 3, 12489 Berlin, Germany

* Corresponding authors: leonor.cueva@uam.es; raquel.caballero@uam.es

Abstract

The sulfurization of co-evaporated $\text{Cu}_2\text{ZnSnSe}_4$ (CZTSe) thin films is studied. In this work, a relationship between the Na concentration and the further S incorporation in the CZTSe absorber layer is found. Na is added by a NaF precursor layer before CZTSe co-evaporation and/or by diffusion from the soda-lime glass substrate. Higher Na concentrations result in bigger grain sizes, higher S/(S+Se) atomic ratios and photovoltaic devices with higher V_{OC} , as investigated by SEM, GIXRD, Raman and I-V measurements. Results using an alternative substrate as ceramic verify the importance of the control of the Na content, which alters the carrier concentrations and elements

distribution with much higher S and Na concentrations at the surface in this particular case. By using this methodology, it is possible to tune the kesterite band gap energy by the creation of S-gradient through the absorber thin film. This may provide a new approach for the control of $\text{Cu}_2\text{ZnSn}(\text{S,Se})_4$ growth and development of high efficiency kesterite solar cells. Efficiencies of 5.5 % and 6.4 % are obtained using ceramic and SLG substrates respectively (without antireflection coatings and without grids).

Keywords: kesterite; solar cells; co-evaporation; sulfurization; Na

1. Introduction

$\text{Cu}_2\text{ZnSn}(\text{S,Se})_4$ (CZTSSe) has been shown as a promising candidate as absorber layer for thin film solar cells. A maximum efficiency of 12.6 % has been achieved [1]. This performance is very low in comparison to the highest conversion efficiency of $\text{Cu}(\text{In,Ga})\text{Se}_2$ (CIGSe) solar cell of 22.9 % [2]. The main limitation of kesterite-based solar cells is the open circuit voltage deficit (defined as $E_g/q - V_{\text{OC}}$, where E_g is the absorber band gap energy, q is the elementary charge and V_{OC} is the open circuit voltage). One of the reasons of this drawback is the non-optimal quality of kesterite absorber and the presence of secondary phases [3, 4]. The existence of electrostatic potential fluctuations in the CZTSSe absorber layer could be another important factor that deteriorates the solar cell efficiency [5, 6]. The interface recombination with the unfavourable alignment of the conduction band minimum (CBM) at the CZTSSe/buffer interface leads to a decreased performance [3].

Goushi et al [7] achieved an enhanced V_{OC} of $\text{Cu}(\text{In,Ga})(\text{S,Se})_2$ (CIGSSe) devices using the sulfurization after selenization (SAS) method. Solar Frontier reported CIGSSe-based solar cells with 22.3 % efficiency using this SAS process [8]. Nowadays, this company has achieved 19.8 % CIGSSe mini-modules using such a method [9]. With

this SAS method, an enlarged surface bandgap by S-incorporation in CIGSe is obtained with a reduction of defects, lowering the valence band maximum (VBM) at the vicinity of the CIGSe surface region. Experimental and modelling results have demonstrated this effect, leading to an enhanced V_{OC} [10, 11]. Nevertheless, it is difficult to apply this method for kesterite absorber layers successfully. It seems that the mechanism of S diffusion into CIGSSe matrix and CZTSSe are quite different. Cai et al [12] have shown that the sulfurization of the surface of the kesterite absorber layer leads to a widening surface bandgap with an improved device performance and V_{OC} . The sulfur-modified surface of kesterite was achieved by introducing H_2S gas during cooling stage of the selenization process of stacked metallic precursors [12].

On the other hand, it is well known that the inclusion of alkali elements in CIGSSe absorber layers enhance the V_{OC} and improve the final photovoltaic devices [2, 13, 14]. Recently, the influence of alkali elements, particularly of Na, on the kesterite absorber layer has been studied [15-20]. However, these effects are still under discussion. First, there is still some controversy in the influence of Na in the grain growth and the crystallization of the absorber layers. Repins et al. [15] reported the improvement of the photovoltaic parameters of co-evaporated kesterite devices by the introduction of a NaF precursor layer without affecting the grain size, as well as Abzeiher et al. [19] found that the larger grain size in solution-based kesterite absorbers are not necessary related with the Na presence. On the contrary, some research groups state the positive effect of the presence of Na, regardless the different Na addition processes, in the crystallization and in the grain growth [16, 20]. Regarding the alkali impact on the photovoltaic parameters, Li et al. [17] showed that the presence of Na causes an increase of the V_{OC} and FF due to an increment of the hole density, making the acceptor levels shallower. However, Na produces lower J_{SC} owing to a narrower depletion width and a decrease in

the carrier lifetime. Xie et al. [18] also reported the importance of Na content and Na in-depth profile, especially in the CZTSSe/CdS region of the solar cells, for the device performance. Very recently, Haass et al [21] has found the importance of the adjustment of Sn content and alkali concentration for each alkali metal, Li, Na, K, Rb and Cs, achieving efficiencies higher than 11 % by using Li. In general, it has been reported the favorable effect of alkali metals in the improvement of kesterite devices, but there is not a clear explanation about the alkali inclusion mechanisms and the final compounds formed. In this regard, Sutter-Fella et al. proposed a selenization mechanism in which the presence of Na raises the chemisorption of Se species forming Na_2Se_x phases that are responsible of the grain growth [20]. Whereas Xie et al. proposed the formation of $\text{Na}_2\text{Se(S)}$ and also Na-containing species with high vapor pressures as Na_2CO_3 , Na_2O or NaSe(S)O_3 , since they observed large Na loss at the absorbers surface [18].

The objective of this work is to investigate the incorporation of S into co-evaporated CZTSe layers without using any $\text{H}_2\text{S}/\text{H}_2\text{Se}$ toxic gases, and to study the role of Na on S incorporation. The sulfurization of CZTSe at 550°C leads to the formation of CZTSSe. Here, we have demonstrated a relationship between the Na added, via diffusion from the substrate or via evaporation of a NaF precursor layer before the co-evaporation process, and the S content incorporated into the kesterite material. In this way, we show a new approach to generate the optimal $\text{S}/(\text{S}+\text{Se})$ ratio and gradient through the kesterite absorber layer. This work shows that the control of Na is a key parameter to enhance V_{OC} and the final CZTSSe-based device performance. Finally, this investigation has been extended to photovoltaic (PV) devices grown on ceramic substrates, increasing the range of applications, for example for Building Integrated PV (BIPV) concepts.

2. Materials and methods

2.1. Deposition of $\text{Cu}_2\text{ZnSn}(\text{S,Se})_4$ thin films

$\text{Cu}_2\text{ZnSnSe}_4$ thin films were deposited onto $5 \times 5 \text{ cm}^2$ Mo/soda-lime glass (SLG) or Mo/ceramic substrates by co-evaporation of Cu, Sn, ZnSe and Se at nominal substrate temperature between $275\text{-}325^\circ \text{C}$. A scheme of the co-evaporation system is shown in Figure 1. The substrates are heated by lamps localized on top of the back substrate side. The substrate temperature was measured by a thermocouple behind the substrate. The temperatures are given as measured in the experimental set-up. The substrate was rotated during deposition to improve the film uniformity. A quartz crystal microbalance was used to determine the Se evaporation rate before starting the process.

The co-evaporation process consisted of three stages. First, Se was evaporated onto Mo/substrate for around 3 minutes. Secondly, all the elements were co-evaporated simultaneously for around 33 minutes. After that, in order to achieve a Cu-poor composition, Sn, ZnSe and Se were co-evaporated the same time as used in the second stage of the co-evaporation process. The low substrate temperature used was to avoid the losses of SnSe. As-grown CZTSe thin films were annealed at 550°C for 30 minutes in Ar atmosphere at pressure of $9.5 \times 10^4 \text{ Pa}$ under excess of sulfur. For that purpose, the as-co-evaporated CZTSe thin films were placed in a partially closed graphite box of $56 \text{ mm} \times 70 \text{ mm} \times 20.5 \text{ mm}$ with a hole of 1 mm diameter in the lid, and inserted into a quartz tube furnace [22]. In order to have an overpressure of sulfur, 22 mg of pure elemental sulfur (99.999 %) were also supplied into the graphite container. The heating rate was of $20^\circ \text{C}/\text{min}$ and the cooling rate was $10^\circ \text{C}/\text{min}$ in all the cases.

Table 1 summarizes the composition measured by Energy Dispersive X-ray spectroscopy (EDX) of the samples grown by different co-evaporation processes.

Samples 1 and 2 come from the same co-evaporation process carried out at nominal substrate temperature of 325° C using different substrate materials, SLG and ceramic respectively. Sample 3 was co-evaporated onto Mo/SLG at lower nominal substrate temperature of 275° C.

As it has been mentioned before, generally, the addition of Na on CZTSSe has a positive effect on the final solar cells. Because of the low substrate temperature used during these co-evaporation processes, and therefore the reduced Na diffusion from the SLG towards the absorber layer, around 15 nm NaF layer was evaporated prior to the CZTSe co-evaporation in the same vacuum chamber at room temperature for samples 1 and 2. The ceramic substrate used in this work is commercial ecological porcelain stoneware ceramics, which was developed using a ceramic paste formulation with the addition of industrial wastes (recycled glass, sludges and chamote). This was coated with vitreous enamels containing quantities of Na₂O corresponding to 1 wt%, which act as Na source. As reported by Becerril-Romero et al. [23], the average roughness lies in the range of 15-20 nm for concentrations between 2 wt % and lower of 20 wt % of Na₂O. Although it is high in comparison to SLG (7 nm), these values are acceptable for PV applications. This alters the surface morphology of the substrates creating undulations, pinholes and cracks. However, in [23], a flat surface was observed for a concentration of Na₂O of 2 wt%. As mentioned above, here we work with enamel containing only 1 wt % of Na₂O and despite the low Na concentration, it is visible the rougher surface of the Mo on the ceramic compared to that on SLG substrate. It is worth mentioning that the higher roughness and thickness of the ceramic substrate than for the SLG produce variations in the Mo layer growth and could lead to a decrease in the nominal temperature of the Mo/ceramic structure during the co-evaporation process.

Sample 3 was grown without adding any extra Na concentration apart from that diffusing from the SLG substrate. For that, we could assume that the Na content obtained from the out-diffusion of the SLG of sample 3 is lower than that of sample 1 deposited at higher substrate temperature and with an extra Na source.

2.2. Device fabrication

Solar cells with the CZTSSe absorber layers were fabricated by using a CdS buffer layer of around 50 nm deposited by chemical bath deposition followed by 50 nm i-ZnO and 350 nm of In₂O₃:SnO₂ deposited by DC-pulsed sputtering to act as a transparent conductive window layer. The absorber layer was etched with (NH₄)₂S before the buffer layer deposition [4]. Sample 3 was divided in different pieces, and on one of them KCN etching (2 wt %, 2 min) was carried out before CdS deposition instead of (NH₄)₂S. The total area of the solar cells was 0.09 cm². The devices had neither grids nor antireflection coating layer. Moreover, no thermal treatment was carried out after finishing the solar cell devices.

2.3. Characterization techniques

The chemical composition was measured by energy dispersive X-ray spectroscopy (EDX) (Oxford instruments, model INCAx-sight) inside a Hitachi S-3000N scanning electron microscope (SEM). EDX measurements were carried out at 25 kV operating voltage, and the Cu K, Zn K, Sn L, Se K and S K lines were used for quantification. Grazing incidence X-ray diffraction (GIXRD) was performed to investigate the structural properties of the CZTSSe thin films. GIXRD data were collected with a PANalytical X'Pert Pro MPD diffractometer, using CuK_α radiation and a multilayer mirror to produce a parallel beam. Detector scans with incident angle of 4° were carried

out. Raman scattering measurements were performed in back scattering configuration using a highly sensitive Raman apparatus developed at IREC consisting in a Horiba Jobin Yvon iRH320 spectrometer coupled with a low noise CCD detector cooled at -70°C . In this system, excitation and light collection were made through a macro optic system with a laser spot diameter of about $70\ \mu\text{m}$. Back-scattering measurements were performed under 532 and 785 nm excitation wavelengths by focusing laser spot directly onto the layer surface which allows the assessment of the absorber layer without any contribution from the upper layers. Excitation power was kept below $26\ \text{W}/\text{cm}^2$ in order to avoid presence of thermal effects in spectra. The first-order Raman spectrum of monocrystalline silicon (Si) was measured as a reference before and after each Raman spectrum acquisition, and spectra were corrected by imposing Si first order at $520\ \text{cm}^{-1}$. In-depth chemical composition profiles were obtained by means of Auger electron spectroscopy (AES) using a Phi 670 Scanning Auger Nanoprobe. The excitation source was a field emission electron gun working at 10 keV and 10 nA, and scanning a surface of 15×15 microns to avoid inhomogeneities. Sputtering was done with Argon ions at 4 keV, and keeping vacuum under 9×10^{-9} Torr to prevent the reabsorption of the sputtered material. MultiPak v.8 and OriginLab 8.0 programs were used for data treatment and actual measurements of own standards were used as references for quantifications purposes.

The distribution of Na within the samples was measured via glow discharge optical emission spectroscopy (GDOES) in a Spectruma GDA 650. Depth profiles are collected by pulsed RF sputtering with Argon plasma. The characteristic emission of the ionized atoms is captured in a CCD array. Measurements on all samples were performed with the same settings in series, therefore intensities can be compared in between samples. However, since the measurements were performed without calibration sample, absolute

Na atomic contents cannot be given. The Na concentration in the samples was quantified by measuring the digested samples in HCl:HNO₃ (1:1) using an inductively coupled plasma mass spectrometry (ICP-MS), NexION 300XX (Perkin Elmer). I-V characteristics were measured using a Sun 3000 class solar simulator (Abet Technologies Inc., Milford, Connecticut, USA). Measurements were carried out at 25° C and under air mass AM1.5 and 100 mW/cm² illumination. External quantum efficiency (EQE) measurements were performed using a Bentham PVE300 system (Bentham Instruments Ltd., Berkshire, UK) calibrated with a Si and Ge photodiode. Reversed voltage-biased EQE curves were collected by connecting a Keithley 2400 source meter (Keithley Instruments Inc., Cleveland, Ohio, USA) directly to the primary coil of the transformer and biasing the device at the desired voltage. Capacitance voltage measurements (C-V) were carried out using a HP 4192A LF impedance analyzer under a frequency of 100 kHz.

3. Results and discussion

The structural properties of samples 1, 2 and 3 after sulfurization were investigated. Figure 2 displays the GIXRD ($GI = 4^\circ$) pattern of such samples. As it can be observed in Figure 2.a., kesterite phase is formed. The presence of the 002, 101 and 110 Bragg peaks confirm unambiguously the existence of CZTSSe phase. Moreover, a reflection at around 31.8° appears, indicating the presence of the Mo(S,Se)₂ layer. In the case of the sample grown on ceramic, the completed device was measured by GIXRD, detecting the reflections corresponding to ITO because of the window layer of the solar cell. No other secondary phases can be detected, although the presence of Zn(S,Se) and Cu₂Sn(S,Se)₃ phases cannot be ruled out since their diffraction reflections coincide with those of CZTSSe. The PDF data for tetragonal Cu₂ZnSnS₄ (No. 01-075-4122) and

tetragonal $\text{Cu}_2\text{ZnSnSe}_4$ (No. 04-010-6295) have been used for identification of the different phases. The partial substitution of Se by S atoms leads to smaller unit cell parameters. Figure 2.b. shows a zoom of the 112 and 103 Bragg peaks of all samples. It is clearly visible that the Bragg peaks of sample 1 grown on SLG substrate are shifted towards higher 2θ angles, indicating a much higher incorporation of S into the CZTSe during the thermal treatment. However, the sample 2 deposited on ceramic substrate presents a very low S concentration as shown by its diffraction peaks, which are very similar to those characteristics of CZTSe. The XRD peaks of sample 3 are between those of sample 1 and 2 with an intermediate S concentration in agreement with EDX measurements. In addition, the $S/(S+Se)$ ratios were calculated from the XRD diffractograms obtaining 0.84, 0.04 and 0.28 for sample 1, 2 and 3 respectively. Although these values are not exactly the same as those obtained by EDX, probably due to differences in the depth of the analysis, the trend agrees well with the EDX results. Additionally, a more detailed analysis of the 112 peak (Figure 2.b.), shows the asymmetry of these signals in all samples suggesting the presence of a slight depth gradient in the $S/(S+Se)$ ratio in the absorber composition.

Raman spectroscopy of all samples was also studied (see Figure 3). First of all, it is confirmed that only kesterite phase is detected on the samples surfaces. There is no evidences of $\text{Zn}(S,Se)$, $\text{Sn}(S,Se)$ and $\text{Cu}_2\text{Sn}(S,Se)_3$ secondary phases using different excitation wavelengths. However, the comparison between all spectra shows clear changes in the Raman fingerprint that are attributed to the different $[S]/([S]+[Se])$ ratios in the absorber layers. Based on reports of Dimitrievska et al. [24, 25], in Figure 3.a. the $[S]/([S]+[Se])$ atomic ratio of the CZTSSe was estimated. $[S]/([S]+[Se])$ atomic ratios of 0.76, 0.29 and 0.08 were determined for samples grown on SLG (sample 1 and 3) and on ceramic (sample 2) respectively. For sample 2, grown on ceramic substrate, a

$[S]/([S]+[Se])$ atomic ratio depth analysis of the first hundreds nanometers has been performed by using different excitation wavelengths in the same region [26]. Under 532 nm and 785 nm excitation wavelengths the S content can be analyzed in the kesterite material for the surface (< 50 nm) and sub-surface (<100 nm) regions. Both Raman spectra, acquired at 532 and 785 nm, exhibit characteristic features of very Se-rich CZTSSe solid, however the results suggest the presence of a slight S-gradient through the first hundreds nanometers of the absorber layer, being S richer at the top of the absorber layer with a $[S]/([S]+[Se])$ atomic ratio of 0.11. Similar analysis has been performed for sample 3 (not shown). On the contrary, for sample 3 a slight S-gradient has been observed but in inverse direction, less S content is observed in the surface (0.27) than in the sub-surface (0.29).

In CIGSSe solar cells, the CBM is almost not affected for moderate S content $[S]/([S]+[Se]) \leq 0.5$ which leads to a more favorable situation than the notch profile usually obtained by Ga surface enrichment [11]. Later, it will be shown that better solar cells are obtained with the sample 3 than with the sample 1.

Auger electron spectroscopy depth profiles were carried out to investigate the distribution of the elements through the absorber layer of the samples. Figure 4.a. and 4.b. show the depth profiles of Cu, Zn, Sn, Se, S and Mo of two representative solar cells coming from the sample 2 (2-c2 and 2-b6). PV parameters of both devices are also displayed. It is important to highlight the S-gradient through the CZTSSe layer with much higher S concentration at the surface, in good agreement with Raman results. At the same time, a decreased Se content is observed at the surface of the absorber layers. It seems that the Se atoms are substituted for the S atoms in the surface region of the CZTSe layer. This phenomenon agrees well with Kobayashi et al's work where CIGSe

thin films deposited by molecular beam epitaxy using a three-stage process were sulfurized using H_2S gas [10].

Despite the similar performance of both devices, the solar cell with higher V_{OC} corresponds to that with higher S content on the surface, as displayed clearly in Figure 4.c. It seems that there is a relationship between the S amount on the surface of the CZTSSe and the V_{OC} of the solar cell. It is evident that the distribution of the elements through the CZTSSe layer is not completely uniform on the $5 \times 5 \text{ cm}^2$ ceramic substrate. The sample 2 plotted in Figure 4.b. is also characterized by an increased Zn concentration and slight decreased Sn content at the surface. However, as mentioned above, the final performances of both devices are very similar.

Figure 5.a. and 5.b. shows the elements distribution of two representative completed devices using sample 1 and 3 as absorber layers respectively, both grown on SLG substrates. It is important to point out the distribution of S across the completed absorber layer, very different from the S depth profile obtained for the sample 2 deposited on ceramic. It is again confirmed the substitution of Se atoms for S atoms in the CZTSe matrix and demonstrated the higher S concentration in sample 1. Not only the S content is different for both samples on SLG, but also the S distribution through the absorber layer despite the same thermal treatment and S amount added. It seems that the Na content plays an important role on the S incorporation on co-evaporated CZTSe thin films. Moreover, the distribution of the other elements can be also affected by the Na concentration and depth profiling. Sun et al. [27] also observed that the redistribution of the metal elements in CZTS was assisted by the presence of Na. From these results, it is important to highlight that higher Na concentrations lead to higher S incorporation into CZTSe lattice during the sulfurization process. As described above, sample 1 was co-evaporated at higher nominal substrate temperature than sample

3; however, both received the same sulfurization process. In addition, a 15 nm NaF precursor layer was added for the sample 1. This was translated in an average Na concentration measured by ICP-MS of 0.82 at % and 0.65 at % for samples 1 and 3 respectively.

Our experimental results indicate that the Na content seems to be one of the key parameters to control the sulfurization of the CZTSe absorber layer, playing an important role in the formation of S-gradient and in the $[S]/([S]+[Se])$ atomic ratios.

With the aim of understanding the Na effect on the kesterite thin films, the Na distribution through the absorber layer was studied by GDOES (see Figure 6). It is important to mention that it is not possible to compare the differences of time (x-axis) of the samples and therefore layers thickness. The main difference observed in Figure 6 is that Na distribution differs depending on the material substrate used. In sample 2 grown on ceramic substrate, the Na-GDOES signal is much higher at the CZTSSe surface. On contrast, in the case of sample 1 (NaF + SLG) and 3 (SLG), a higher Na-GDOES signal is detected next to the Mo back contact, especially for sample 1, as observed in [17].

It seems that the sulfurization process affects differently the CZTSe grown on ceramic. It has been reported [18] that post-thermal treatments of CZTSSe onto Mo/SLG substrates at high temperatures (above 400°C) accelerates both, the Na diffusion rate and the loss rate of Na, causing higher Na accumulations at the interface between the Mo and the kesterite absorber and less Na content at the surface due to an increase in the Na loss rate. As it has been mentioned above, in this work the sulfurization process is performed at 550° C in all cases. Thus, the sulfurization temperature is high enough to have Na accumulations at the back and at the surface of the absorber layers, but this is not the case for the ceramic substrate. Although we should take into account that the different surface roughness of both type of substrates makes different Mo layer growth

with a possible formation of different CZTSSe/Mo back interface. The most important feature that might be affecting the Na distribution is the amount of thermally activated Na available (see Figure 7). In the case of sample 2, the available Na content practically only comes from the NaF precursor layer, which diffuses towards the surface layer reacting with S at 550° C. In samples 1 and 3, the initial Na content in the absorber layers diffuses towards the surface as in the case of sample 2, but also the high temperature raises the Na out-diffusion from the SLG during the whole sulfurization process supplying continuously thermally activated Na atoms to the CZTSe layer (see Figure 7). As it has been shown before, sample 1 presents higher Na and S contents than sample 3. This fact is probably due to the two Na sources in sample 1 that increase the Na content, the one that comes from the NaF layer and the other one that comes from the SLG substrate. The latter could be the reason why the S is incorporated through the whole absorber layer when using SLG substrates instead of mainly remaining at the surface layer as in the case of the ceramic substrate.

Moreover, Abzieher et al. [19] reported that Na can also be transported via the gas phase during selenization. Based on [19-20], a polyselenide phase like Na_2Se_x (g) may be formed on the surface of the thin films during the co-evaporation process. XPS measurements have been carried out on sample 1. Na 1s peak has been detected on the surface. Unfortunately, it is not possible to corroborate the formation of Na-Se and/or Na-S bonds due to the overlapping of Na KLL Auger peak and Sn 3d (not shown here). On the other hand, it has been reported that Na neutralizes the donor defect V_{Se} in CIGSe solar cells [28], increasing the p-type conductivity and carrier concentration. Here, we have observed that the higher Na concentration implies the higher S incorporation into CZTSe, forming the pentanary $\text{Cu}_2\text{ZnSn}(\text{S}_x\text{Se}_{1-x})_4$. It seems that Na promotes the partial substitution of Se for S (Figure 5 and 6), replacing the possible Se

vacancies by S, increasing the band gap energy and the carrier concentration of the kesterite material.

Gathering these results, we proposed the following mechanism (see Figure 7): (i) The initial Na concentration located in the absorber layers of both types of substrates diffused toward their surfaces during the sulfurization at 550° C. (ii) At the same time, in the case of sample 1 and 3, the continuously input of thermally activated Na atoms from the out-diffusion of the SLG substrates result in a higher Na concentration at the Mo/CZT(S)Se interface and produce the incorporation of S inside the absorber layer due to the incessant reaction and diffusion to the surface.

This is a proposal based on the experimental results obtained. However, GDOES depth profile measurements cannot discriminate if Na is located at the grain boundaries or inside the grains. Further experiments are necessary for that.

Figure 8 shows the cross-sectional SEM images of samples 1, 2 and 3. Larger CZTSSe grains are observed for sample 1. Sample 3 is characterized by a smaller grain size with some holes between them. No real differences between the device 3 etched with $(\text{NH}_4)_2\text{S}$ and KCN can be observed. It is known that Na is beneficial for the crystallization and leads to larger grain size [20]. The higher nominal substrate temperature together with the incorporation of 15 nm NaF explains the bigger grain size for sample 1 than for sample 3. As mentioned above, the surface morphology of the substrate plays a crucial role for the growth of the different layers composing the PV device. The smaller grain size of the device corresponding to sample 2 can be explained by a lower Na concentration than for the device 1. Furthermore, ceramic substrates seem to respond differently to the thermal sulfurization process since much less incorporation of S takes place for this sample in comparison to sample 1, as demonstrated by GIXRD, Raman and AES spectra. Moreover, the higher content of S at

the surface of CZTSSe on ceramic coincides with the higher Na signal in that region. This different behavior is not only reflected in the grain size, but also in the formation of a thinner absorber layer. Becerril et al. [23] also detected a different behavior of kesterite layers grown on ceramic and SLG during the selenization process.

Table 2 shows the PV parameters together with the band gap energy of the three samples investigated. Sample 1 is characterized for the highest V_{OC} and the lowest short circuit current density (J_{sc}) and fill factor (FF), producing the lower efficiency of 3.5 %. This fact can be related to the higher series resistance (R_s) of $17.1 \Omega \cdot \text{cm}^2$, as shown in Table 2. The much higher V_{OC} can be explained by the higher S and Na concentrations in the bulk of the absorber layer. Samples 2 and 3 with lower S and Na contents present higher J_{sc} and FF, which are responsible for the higher performances of 5.5 % and 6.4 % respectively (J-V curves are shown in Figure 9.a.). The device performances achieved for sample 3 using both chemical etchings are similar. A slight enhanced efficiency solar cell is obtained using KCN etching, which could be related to the possible formation of some Cu-(S,Se) phases because of its higher Cu content.

Another aspect to emphasize is that no the larger CZTSSe grain size corresponds to the highest efficiency solar cell (see Figure 8). Similar results were reported for CIGSe technology, in which no the larger grain size implies the best device performance [29]. Figure 9.b. displays EQE spectra of the devices presented in Table 2. The optical band gap energy (E_g) was extracted from the inflection point of the EQE spectrum in the long wavelength range. $E_g = 1.50 \text{ eV}$, 1.00 eV and 1.17 eV (1.15 eV with $(\text{NH}_4)_2\text{S}$ chemical etching) have been determined for samples 1, 2 and 3 respectively. The high incorporation of S on the sample 1 results in an E_g expected for CZTS and the low incorporation of S for the sample grown on ceramic leads to band gap energy in the range of CZTSe devices. Moreover, the V_{OC} -deficit is of 928 mV, 676 mV and 748 mV

for samples 1, 2 and 3 respectively (734 mV for sample 3 with $(\text{NH}_4)_2\text{S}$ etching). Higher S concentration leads to a larger V_{OC} -deficit, in agreement with the literature [30]. An increased V_{OC} loss with the band gap energy of CZTSSe has been already observed [30]. The V_{oc} -deficit of 928 mV for sample 1 is in the same range as that obtained by IBM for CZTSSe with E_g of around 1.5 eV [31]. On the other hand, the sulfur gradient developed with higher S content at the surface for sample 2 is characterized by the lower open circuit voltage deficit. However, not the best efficiency has been achieved for the devices using sample 2 as absorber layer. These results confirm that the higher device performance is not a result of the higher Na concentration. Therefore, a control of the Na content is a key parameter to create the appropriated S-gradient and S content that leads to higher kesterite solar cell efficiencies.

When comparing reverse-biased EQE measurement with the EQE without bias (see Figure 9.c., the device corresponding to sample 1 shows an increase in collection for the long wavelengths with negative bias (-1 V). The depletion width increases and therefore, improves the electrons collection generated deeper in the bulk of the CZTSSe by applying a reverse-bias voltage. Such behavior is usually explained by poor collection toward the back of the absorber layer [32]. This explains the low J_{SC} for such a device. The difference between reverse-biased EQE with the EQE without bias is less significant for sample 3, which presents higher carrier collection in the long wavelength and thus a higher J_{SC} .

Figure 10 displays C-V spectra of all samples. The depletion width (w_d) of the devices at a bias of 0 V is approximately of 0.28 μm , 0.35 μm and 0.20 μm corresponding to sample 1, sample 2 and sample 3 respectively. A carrier concentration N_{CV} of $3.5 \times 10^{16} \text{ cm}^{-3}$, $9.5 \times 10^{15} \text{ cm}^{-3}$ and $1.1 \times 10^{17} \text{ cm}^{-3}$ can be extracted for solar cells corresponding to sample 1, sample 2 and sample 3 respectively. Li et al. [17] reported similar results in

which the inclusion of Na increases the hole density and thus, the carrier density producing changes in the bulk CZTSe Fermi level. This change leads to higher built-in voltage and therefore to higher V_{OC} values, as in the case of our samples. The depletion width of the sample 1 is reduced in comparison to that of sample 2 (coming from the same co-evaporation process), which is an indication of an increased carrier concentration. This would likely increase the V_{oc} and reduce the J_{sc} since the photocurrent collection may be less efficient in a narrower depletion width, in agreement with our results (see Table 2). However, the sample 3 presents the highest carrier concentration N_{CV} , despite the Na content. Yan et al. [33] observed that the carrier concentration of CZTS solar cells depends on $[Cu]/[Sn]$ atomic ratio. A lower Cu concentration leads to a lower N_{CV} and higher w_d . This is in agreement with our results (see Table 1). Therefore, the higher V_{OC} for sample 1 cannot be only related to doping concentrations, but it can be explained by the higher S concentration. Na-doped CZTSe solar cells of 11.6 % efficiency and fabricated using a NaF precursor layer and by diffusion from SLG substrates were characterized by $w_d = 0.23 \mu m$ and $N_{CV} = 1 \times 10^{16} cm^{-3}$ [34]. One of the reasons of the much lower efficiency of sample 1 is due to the high S concentration through the whole absorber layer. It is known that high efficiencies are achieved for CZTSSe with low S content. The world record CZTSSe solar cell presents a $[S]/([S]+[Se])$ atomic ratio of only 0.1 [1].

All these results show that the Na content increases the S amount and produces its incorporation through the whole CZTSe absorber layer in the case of SLG substrates. As expected, this fact has a huge impact in the optical band gap energy of the kesterite material. It is important to highlight that it should exist a Na concentration limit that may allow us to incorporate the appropriate S content and depth profiling that enhance V_{OC} without harming the J_{SC} and improving the final efficiency of kesterite devices.

4. Conclusions

CZTSSe thin films have been grown by sulfurization of co-evaporated CZTSe layers. Based on our experimental results, Na seems to play an important role for the development of S-gradient and $[S]/([S]+[Se])$ atomic ratios, which affect the properties of the kesterite material and solar cells. A higher Na concentration results in a higher S incorporation into the CZTSe matrix, leading to higher band gap energies and V_{OC} . Efficiencies of 5.5 % and 6.4 % have been obtained using ceramic and SLG substrates respectively. These results provide an interesting and new approach to control the CZTSSe growth, which will help to further improve the synthesis process and kesterite-based devices performance.

Acknowledgments

This work was supported by MINECO project (WINCOST, ENE2016-80788-C5-2-R). LC acknowledges financial support from Community of Madrid (Empleo Juvenil, PEJD-2016/IND-2238) and RC also acknowledges financial support from Spanish MINECO within the Ramón y Cajal program (RYC-2011-08521). The authors would like to thank J. Cardá's group from Universitat Jaume I for the supply of ceramic substrate.

References

- [1] W. Wang, M.T. Winkler, O. Gunawan, T. Gokmen, T.K. Todorov, Y. Zhu, D.B. Mitzi, Device characteristics of CZTSSe thin-film solar cells with 12.6% efficiency, *Adv. Energy Mater.* 4 (2014) 1301465.
- [2] Solar Frontier K.K. “Solar Frontier achieves world record thin-film solar cell efficiency: 22.9%”, press release, http://www.solar-frontier.com/eng/news/2017/1220_press.html, (accessed 20 December 2017).
- [3] X. Liu, Y. Feng, H. Cui, F. Liu, X. Hao, G. Conibeer, D.B. Mitzi, M. Green, The current status and future prospects of kesterite solar cells: a brief review, *Progr. Photovolt. Res. Appl.* 24 (2016) 879-898.
- [4] H. Xie, Y. Sánchez, S. López-Marino, M. Espíndola-Rodríguez, M. Neuschitzer, D. Sylla, A. Fairbrother, V. Izquierdo-Roca, A. Pérez-Rodríguez, E. Saucedo, Impact of Sn(S,Se) Secondary Phases in $\text{Cu}_2\text{ZnSn(S,Se)}_4$ Solar Cells: a Chemical Route for Their Selective Removal and Absorber Surface Passivation, *ACS Appl. Mater. Interfaces.* 6 (2014) 12744-12751.
- [5] T. Gokmen, O. Gunawan, D.B. Mitzi, Semi-empirical device model for $\text{Cu}_2\text{ZnSn(S,Se)}_4$ solar cells, *Appl. Phys. Lett.* 105 (2014) 033903.
- [6] J. Scragg, J. Larsen, M. Kumar, C. Persson, J. Sandler, S. Siebentritt, C. Plätzer-Björkman, Cu-Zn disorder and bandgap fluctuations in $\text{Cu}_2\text{ZnSn(S,Se)}_4$: Theoretical and experimental investigations, *Phys. Status Solidi B* 253 (2016) 247-254.
- [7] Y. Goushi, H. Hakuma, K. Tabuchi, S. Kijima, K. Kushiya. Fabrication of pentanary Cu(In,Ga)(Se,S)_2 absorbers by selenization and sulfurization, *Sol. Energy Mat. And Sol. Cells* 93 (2009) 1318-1320.

- [8] Solar Frontier K.K. “Solar Frontier achieves world record thin-film solar cell efficiency: 22.3%”, press release, www.solar-frontier.com/eng/news/2015/C051171.html, (accessed 8 December 2015).
- [9] T. Kato, A. Handa, T. Yagioka, T. Matsuura, K. Yamamoto, S. Higashi, J.-L. Wu, K. F. Tai, H. Hiroi, T. Yoshiyama, T. Sakai, H. Sugimoto, Enhanced Efficiency of Cd-Free Cu(In,Ga)(Se,S)₂ Minimodule Via (Zn,Mg)O Second Buffer Layer and Alkali Metal Post-Treatment. *IEEE J. Photovolt.* 7 (2017) 1773 – 1780.
- [10] T. Kobayashi, H. Yamaguchi, Z.J.L. Kao, H. Sugimoto, T. Kato, H. Hakuma, T. Nakada, Impacts of surface sulfurization on CuIn_{1-x}Ga_xSe₂ thin-film solar cells, *Prog. Photovolt. Res. Appl.* 23 (2015) 1367-1374.
- [11] Z.J.L. Kao, T. Kobayashi, T. Nakada, Modeling of the surface sulfurization of CIGSe-based solar cells, *Solar Energy* 110 (2014) 50-55.
- [12] C.-H. Cai, S.-Y. Wei, W.-C. Hang, C.-H. Hsu, W.-H. Ho, C.-H. Lai, Efficiency enhancement for Cu₂ZnSn(S,Se)₄ solar cells by S-modified surface layer, *Sol. Energy Sol. Cells* 162 (2017) 21-29.
- [13] P. Jackson, D. Hariskos, R. Wuerz, W. Wischmann, M. Powalla, Compositional investigation of potassium doped Cu(In,Ga)Se₂ solar cells with efficiencies up to 20.8%, *Phys. Status Solidi RRL* 8 (2014) 219-222.
- [14] R. Caballero, C.A. Kaufmann, T. Eisenbarth, A. Grimm, I. Laueremann, T. Unold, R. Klenk, H.W. Schock, Influence of Na on Cu(In,Ga)Se₂ solar cells grown on polyimide substrates at low temperature: Impact on the Cu(In,Ga)Se₂/Mo interface, *Appl. Phys. Lett.* 96 (2010) 092104.
- [15] I. Repins, C. Beall, N. Vora, C. DeHart, D. Kuciauskas, P. Dippo, B. To, J. Mann, W.-C. Hsu, A. Goodrich, R. Noufi, Co-evaporated Cu₂ZnSnSe₄ films and devices, *Sol. Energy Mater. Sol. Cells* 101 (2012) 154-159.

- [16] W.M.H. Oo, J.L. Johnson, A. Bhatia, E.A. Lund, M.M. Nowell, M.A. Scarpulla, Grain Size and Texture of $\text{Cu}_2\text{ZnSnS}_4$ Thin Films Synthesized by Cosputtering Binary Sulfides and Annealing: Effects of Processing Conditions and Sodium, *J. Electron. Mater.* 40 (2011) 2214-2221.
- [17] J.V. Li, D. Kuciauskas, M.R. Young, I. L. Repins, Effects of sodium incorporation in Co-evaporated $\text{Cu}_2\text{ZnSnSe}_4$ thin-film solar cells, *Appl. Phys. Lett.* 102 (2013) 163905.
- [18] H. Xie, S. López-Marino, T. Olar, Y. Sánchez, M. Neuschitzer, F. Oliva, S. Giraldo, V. Izquierd-Roca, I. Lauermann, A. Pérez-Rodríguez, E. Saucedo, Impact of Na dynamics at the $\text{Cu}_2\text{ZnSn}(\text{S},\text{Se})_4/\text{CdS}$ interface during post low temperature treatment of absorbers, *Appl. Mater. Interfaces* 8 (2016) 5017-5024.
- [19] T. Abzieher, T. Schnabel, M. Hetterich, M. Powalla, E. Ahlswede, Source and effects of sodium in solution-processed kesterite solar cells, *Phys. Status Solidi A* 213 (2016) 1039-1049.
- [20] C.M. Sutter-Fella, J.A. Stückelberger, H. Hagendorfer, F.L. Mattina, L. Kranz, S. Nishiwaki, A.R. Uhl, Y.E. Romanyuk, A.N. Tiwari, Sodium Assisted Sintering of Chalcogenides and Its Application to Solution Processed $\text{Cu}_2\text{ZnSn}(\text{S},\text{Se})_4$ Thin Film Solar Cells, *Chem. Mater.* 26 (2014) 1420-1425.
- [21] S.G. Haass, C. Andres, R. Figi, C. Schreiner, M. Bürki, Y.E. Romanyuk, A.N. Tiwari, Complex Interplay between Absorber Composition and Alkali Doping in High-Efficiency Kesterite Solar Cells, *Adv. Energy Mater.* (2017) 1701760.
- [22] R. Caballero, J.M. Cano-Torres, E. Garcia-Llamas, X. Fontané, A. Pérez-Rodríguez, D. Greiner, C.A. Kaufmann, J.M. Merino, I. Victorov, G. Baraldi, M. Valakh, I. Bodnar, V. Izquierdo-Roca, M. León, Towards the growth of Cu_2ZnSn_1 .

- $x\text{Ge}_x\text{S}_4$ thin films by a single-stage process: Effect of substrate temperature and composition. *Sol. Energy Mater. Sol. Cells* 139 (2015) 1-9.
- [23] I. Becerril-Romero, S. Giraldo, S. López-Marino, M. Placidi, Y. Sánchez, D. Sylla, A. Pérez-Rodríguez, E. Saucedo, P. Pistor, Vitreous enamel as sodium source for efficient kesterite solar cells on commercial ceramic tiles, *Sol. Energy Mater. Sol. Cells* 154 (2016) 11-17.
- [24] M. Dimitrievska, A. Fairbrother, X. Fontané, T. Jawhari, V. Izquierdo-Roca, E. Saucedo, A. Pérez-Rodríguez, *Appl. Phys. Lett.* 104 (2014) 021901.
- [25] M. Dimitrievska, G. Gurieva, H. Xie, A. Carrete, A. Cabot, E. Saucedo, A. Pérez-Rodríguez, S. Schorr, V. Izquierdo-Roca, Raman scattering quantitative analysis of the anion chemical composition in kesterite $\text{Cu}_2\text{ZnSn}(\text{S}_x\text{Se}_{1-x})_4$ solid solutions, *J. Alloys Compd.* 628 (2015) 464–470.
- [26] F. Oliva, S. Kretzschmar, D. Colombara, S. Tombolato, C.M. Ruiz, A. Redinger, E. Saucedo, C. Broussillou, T.G. de Monsabert, T. Unold, P.J. Dale, V. Izquierdo-Roca, A. Pérez-Rodríguez, Optical methodology for process monitoring of chalcopyrite photovoltaic technologies: Application to low cost $\text{Cu}(\text{In,Ga})(\text{S,Se})_2$ electrodeposition based processes, *Sol. Energy Mater. Sol. Cells* 158 (2016) 168–183.
- [27] K. Sun, F. Liu, C. Yan, F. Zhou, J. Huang, Y. Shen, R. Liu, X. Hao, Influence of sodium incorporation on kesterite $\text{Cu}_2\text{ZnSnS}_4$ solar cells fabricated on stainless steel substrates, *Sol. Energy Mater. Sol. Cells* 157 (2016) 565-571.
- [28] L. Kronik, D. Cahen, H.W. Schock, Effects of Sodium on Polycrystalline $\text{Cu}(\text{In,Ga})\text{Se}_2$ and Its Solar Cell Performance, *Adv. Mater.* 10 (1998) 31-36.
- [29] D. Abou-Ras, R. Caballero, C.A. Kaufmann, M. Nichterwitz, K. Sakurai, S. Schorr, T. Unold, H. W. Schock, Impact of the Ga concentration on the microstructure of $\text{CuIn}_{1-x}\text{Ga}_x\text{Se}_2$, *Phys. Stat. Sol. RRL* 2 (2008) 135-137.

- [30] S. Kim, K.M. Kim, H. Tampo, H. Shibata, K. Matsubara, S. Niki, Ge-incorporated $\text{Cu}_2\text{ZnSnSe}_4$ thin-film solar cells with efficiency greater than 10%, *Sol. Energy Mater. Sol. Cells* 144 (2016) 488-492.
- [31] S. Kim, K.M. Kim, H. Tampo, H. Shibata, S. Niki, Improvement of voltage deficit of Ge-incorporated kesterite solar cell with 12.3 % conversion efficiency, *Appl. Phys. Express* 9 (2016) 102301.
- [32] R. Scheer, H.W. Schock, *Chalcogenide Photovoltaics*. Weinheim, Germany: Wiley-VCH Verlag, 2011.
- [33] K. Yang, J.-H. Sim, D.-H. Son, D.-H. Kim, G.Y. Kim, W. Jo, S. Song, J.H. Kim, D. Nam, H. Cheong, J.-K. Kang, Effects of the compositional ratio distribution with sulfurization temperatures in the absorber layer on the defect and surface electrical characteristics of $\text{Cu}_2\text{ZnSnS}_4$ solar cells, *Prog. Photovolt: Res. Appl.* 23 (2015) 1771-1784.
- [34] Y.S. Lee, T. Gershon, O. Gunawan, T.K. Todorov, T. Gokmen, T. Virgus, S. Guha, $\text{Cu}_2\text{ZnSnSe}_4$ thin-film solar cells by thermal co-evaporation with 11.6 % efficiency and improved minority carrier diffusion length. *Adv. Energy Mater.* 5 (2015) 1401372.

TABLES.

Table 1. Composition and thickness of NaF precursor layer of the samples grown on SLG substrate.

Sample	NaF(nm)	Cu(at%)	Zn(at%)	Sn (at%)	Se(at%)	S(at%)	Cu/(Zn+Sn)	Zn/Sn	S/(Se+S)	(Se+S)/M
1	15	20.2	12.5	12.2	8.60	44.1	0.83	0.98	0.84	1.19
3	-	23.5	12.7	13.2	31.5	19.1	0.91	0.96	0.38	1.02

Table 2. Photovoltaic parameters and band-gap energy of the different CZTSSe solar cell devices.

Sample	Etching	V _{oc} (mV)	J _{sc} (mA/cm ²)	FF (%)	η (%)	R _s (Ω·cm ²)	R _{sh} (Ω·cm ²)	E _g (eV)
1	(NH ₄) ₂ S	572	14.9	40.7	3.5	17.1	179.4	1.50
2	(NH ₄) ₂ S	324	27.6	60.9	5.5	0.3	142.2	1.00
3	(NH ₄) ₂ S	416	25.1	58.5	6.1	0.6	143.8	1.15
	KCN	422	25.9	58.2	6.4	0.6	97.7	1.17

LIST OF FIGURE CAPTIONS

Figure 1. Illustration of the high vacuum co-evaporation chamber.

Figure 2. (a) Grazing incidence ($GI = 4^\circ$) X-ray diffraction spectra of samples 1, 2 and 3. (b) Zoom of the spectra corresponding to 112 and 103 Bragg peaks for all samples.

Figure 3. Raman spectra of (a) samples 1, 2 and 3 at 785 nm excitation wavelength and (b) sample 2 acquired under different excitation wavelengths (corresponding to different penetration depths, thus surface and sub-surface regions can be studied).

Figure 4. (a) and (b) AES depth profiles of CZTSSe/Mo corresponding to two devices of sample 2 (2-c2 and 2-b6). (c) Comparison of S depth profile on the surface of the absorber layer of two solar cells with different PV parameters. A correlation between V_{OC} and S content on the surface seems to occur.

Figure 5. AES depth profiles of the ITO/i-ZnO/CdS/CZTSSe/Mo structure corresponding to the sample 1 (a) and sample 3 (b) absorbers grown on SLG.

Figure 6. Na-GDOES depth profiling of sample 1, sample 2 and sample 3. The absorber layer limits (represented by colored dash lines) are used to simplify visualization of the interfaces.

Figure 7. Proposed mechanism of sulfurization of co-evaporated CZTSe layers growth on ceramic and SLG, corresponding to sample 1 (middle row), sample 2 (upper row) and sample 3 (bottom row).

Figure 8. Cross-sectional SEM micrographs of the completed devices 1, 2 and 3 (etched with $(NH_4)_2S$ and KCN).

Figure 9. J-V curves of the best solar cells of samples 2 and 3 measured in the dark and under illumination (a). Unbiased EQE curves (b) and the ratios between voltage biased (-1 V) and unbiased EQE (c) for the solar cells of Table 2.

Figure 10. C-V spectra of representative devices of all samples.

Figure 1

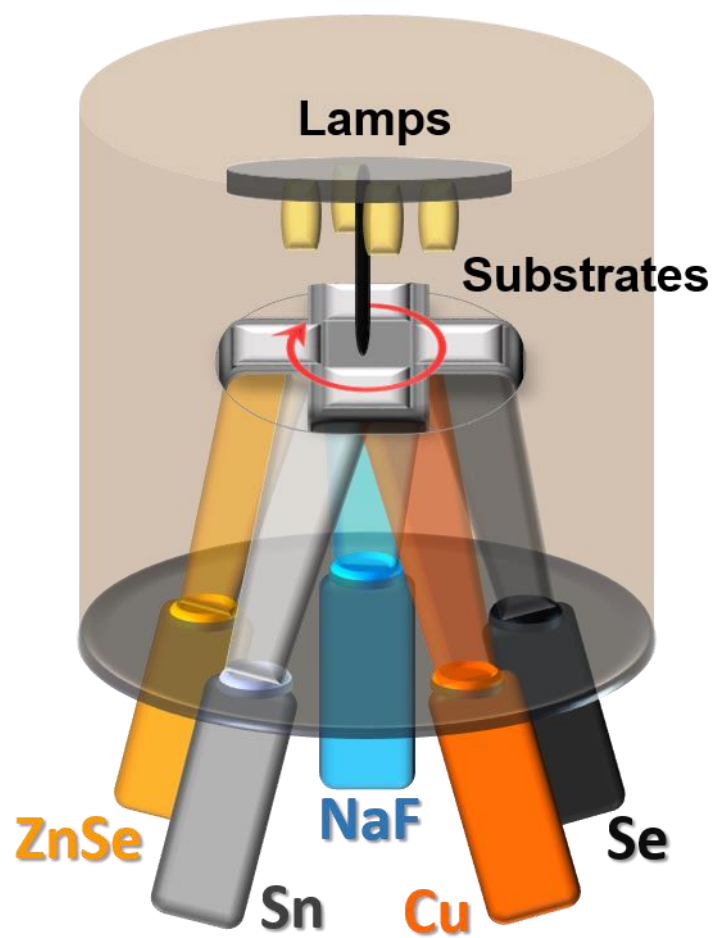


Figure 2

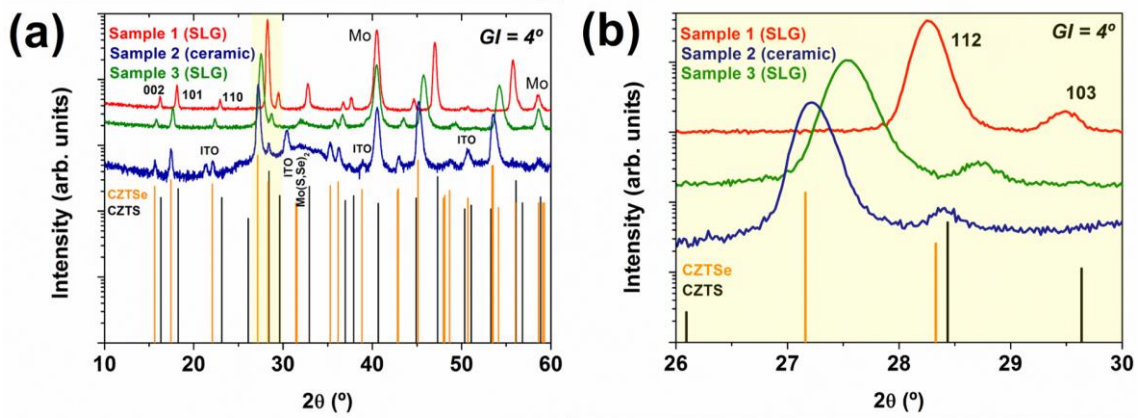


Figure 3

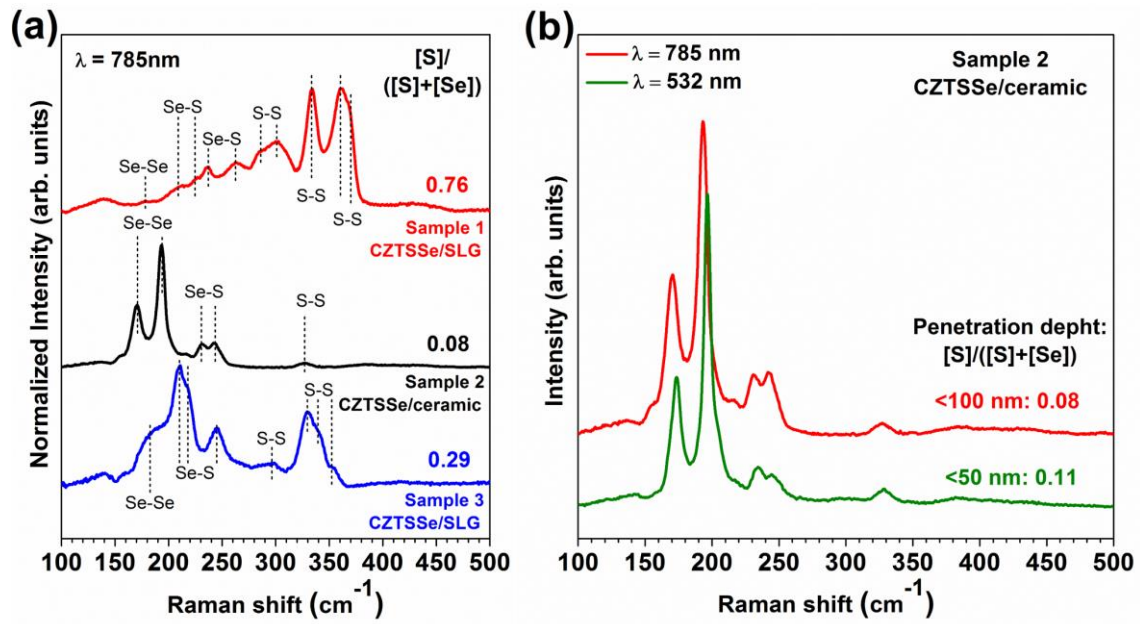


Figure 4

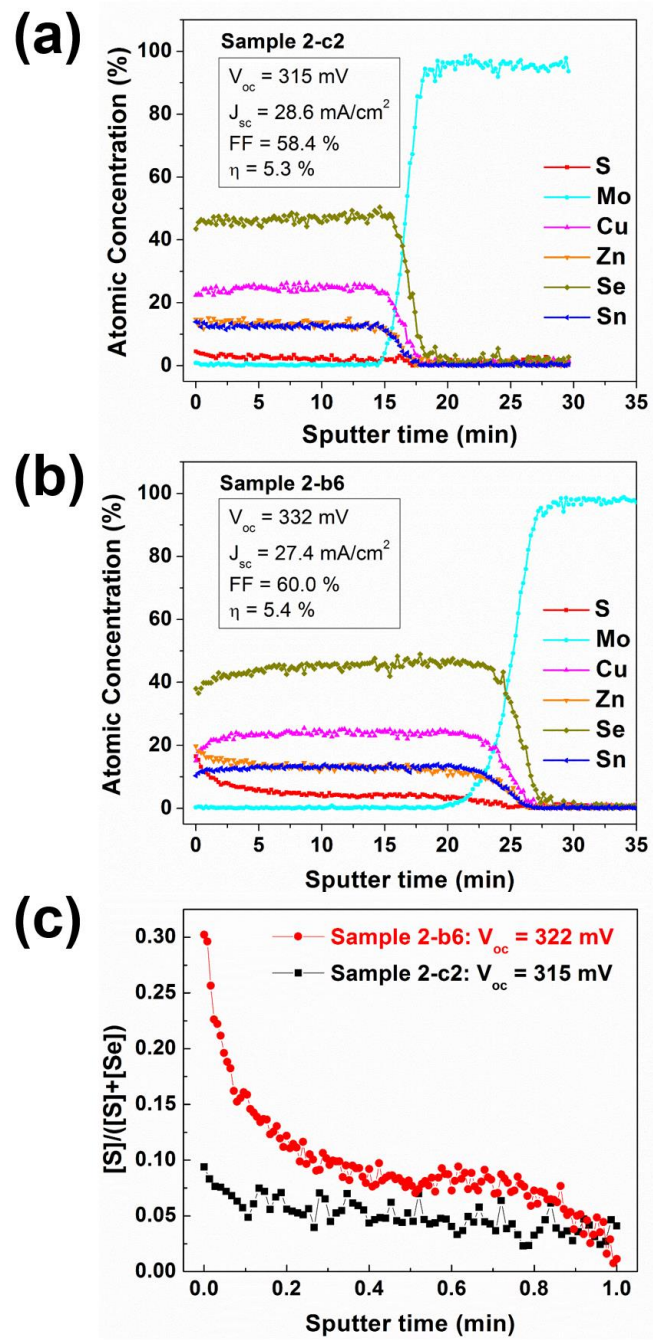


Figure 5

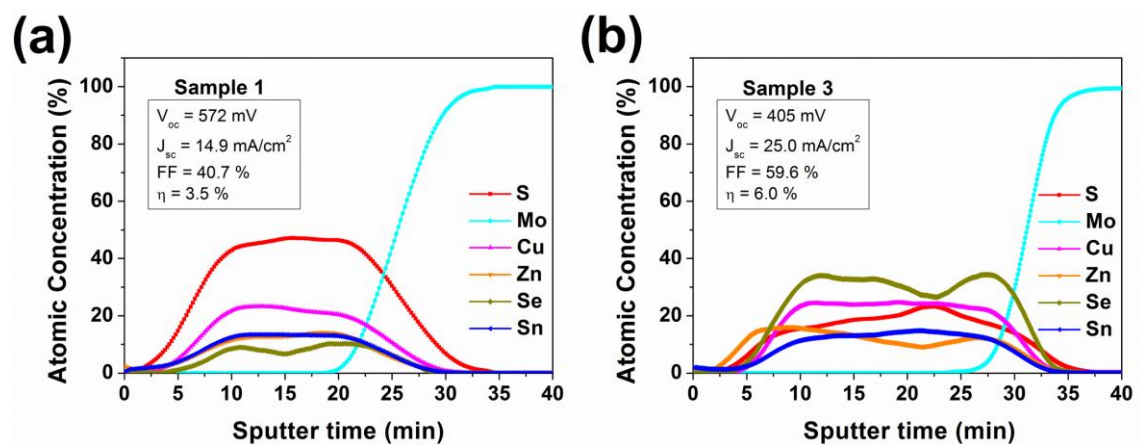


Figure 6

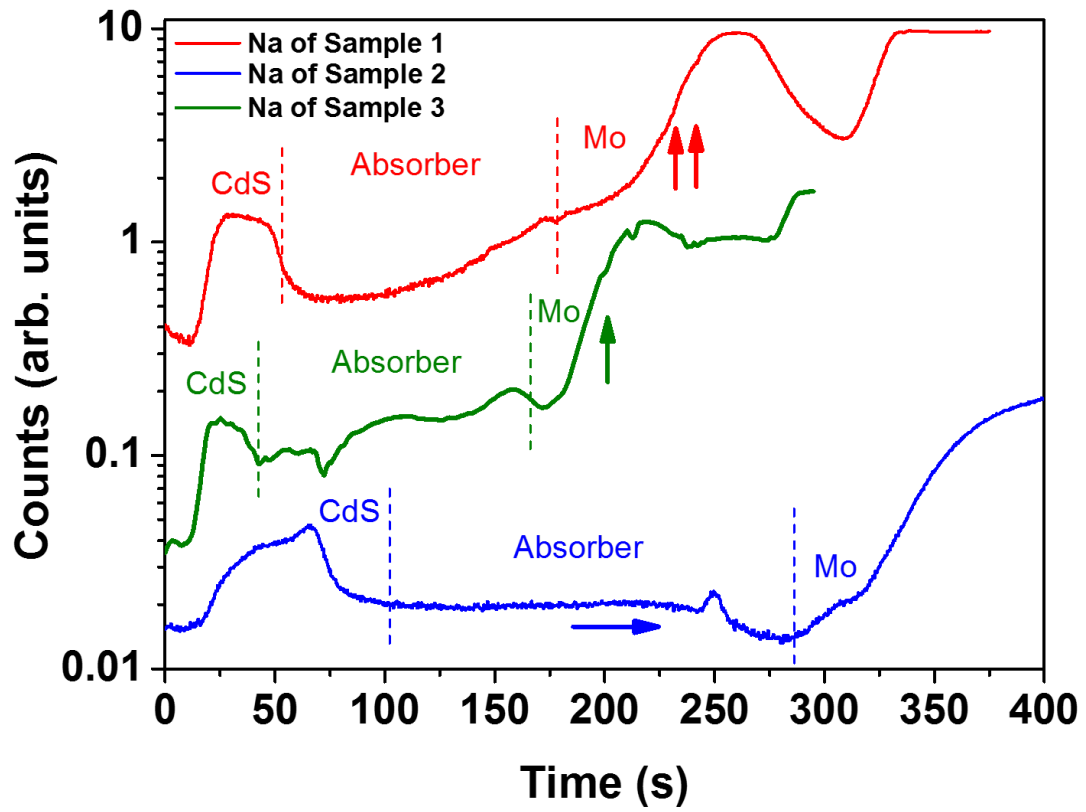


Figure 7

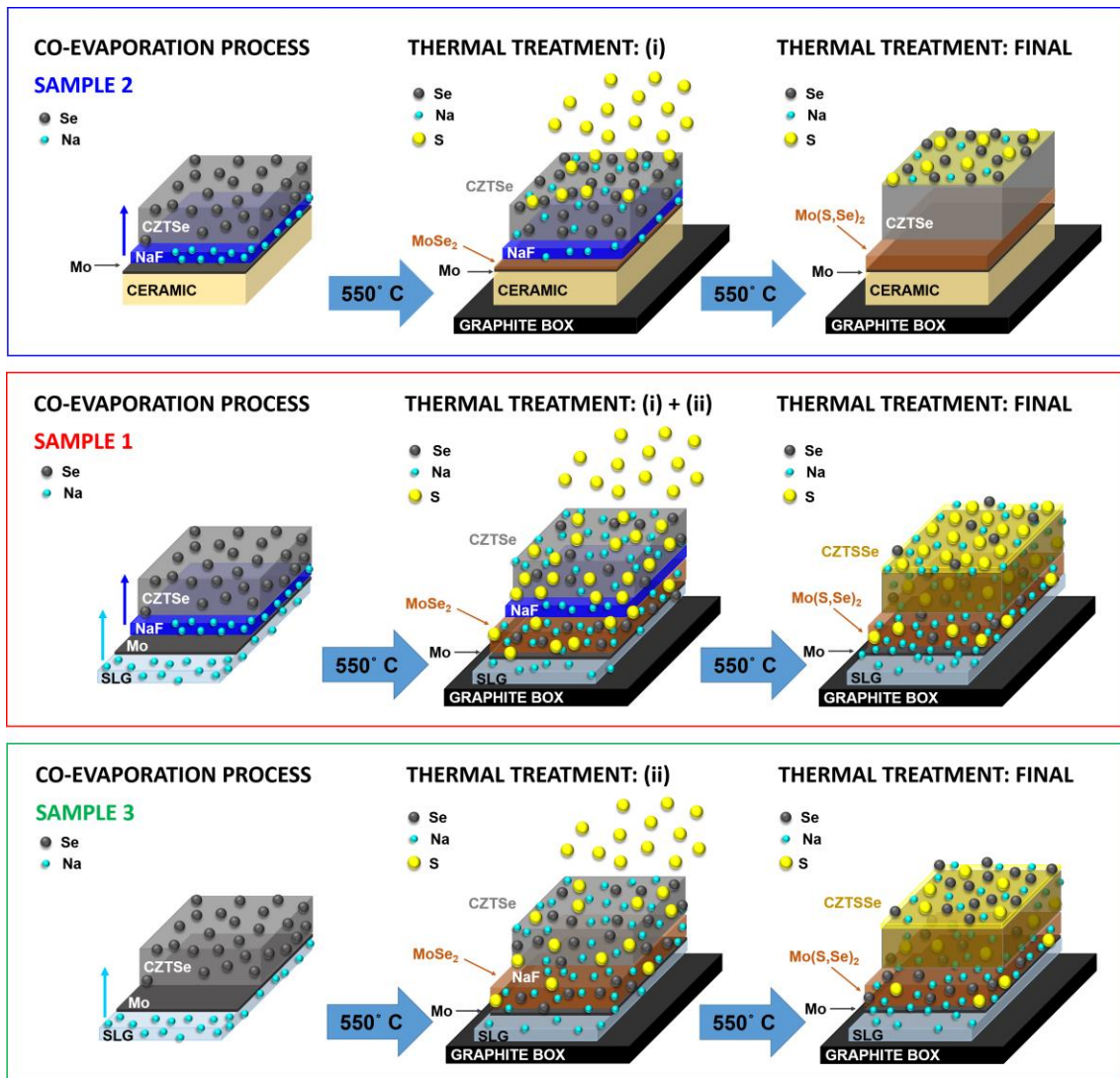


Figure 8

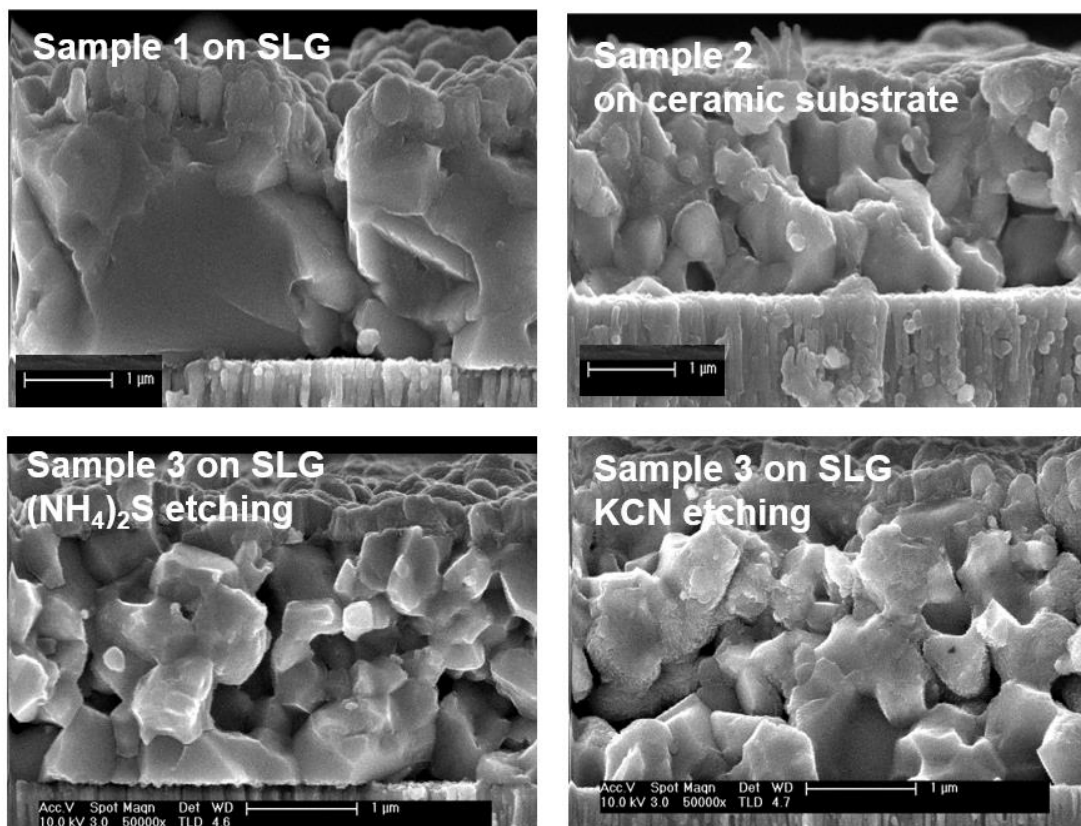


Figure 9

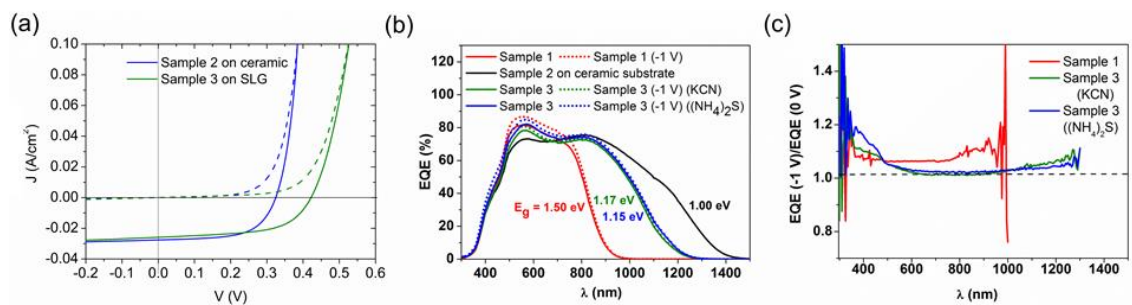
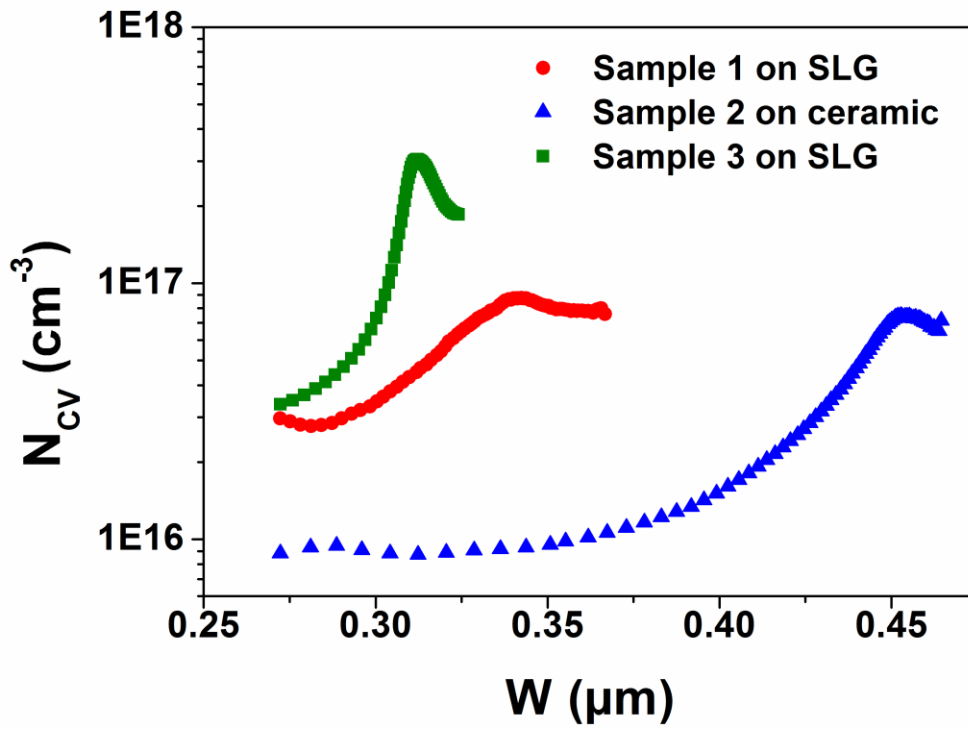


Figure 10



GRAPHICAL ABSTRACT

